ELSEVIER

Available online at www.sciencedirect.com

SCIENCE DIRECT®

Physica D 209 (2005) 49–61

PHYSICA D

www.elsevier.com/locate/physd

Unstable spreading of a fluid filament on a vertical plane: Experiments and simulations

J. Diez[a,1,*], A.G. González[a,1], J. Gomba[a,2],
R. Gratton[a,1], L. Kondic[b]

[a] Instituto de Física Arroyo Seco, Universidad Nacional del Centro de la Provincia de Buenos Aires, Pinto 399, 7000 Tandil, Buenos Aires, Argentina
[b] Department of Mathematical Sciences and Center for Applied Mathematics and Statistics, New Jersey Institute of Technology, Newark, NJ 07102, USA

Abstract

We present results of experiments and numerical simulations on the spreading of a constant volume (CV) of fluid flowing down a vertical plate in the form of a micrometric thin film. In the experiments, the initial condition is generated from a horizontal fluid filament (PDMS) of typical diameter ≈ 0.4 mm, and the flow is probed with two optical techniques: one based on an anamorphic system, and the other on the schlieren method. The first one yields the thickness profile and the second one captures the bidimensional pattern of the transversal film instability. The numerical simulations are performed under the lubrication approximation and using a precursor film to overcome the contact line divergence. The comparison between numerical and experimental profiles shows a very good agreement, and therefore allows to estimate the thickness of the precursor film needed to model the flow. We find that this thin precursor (of thickness 43 nm) is very demanding for the numerical description of the instability, since it requires the use of a very fine grid. We show that the use of thicker precursor allows to obtain numerical results which describe qualitatively well the experimental data. In order to study the early times of the instability, we develop a linear model to account for the evolution of the modal amplitudes of the spatial Fourier spectrum of the contact line of the advancing front (frontline). The model is in good agreement with both experiments and simulations for the appropriate precursor film thickness in each case. We find that the precursor film thickness mainly influences the growth rates of the unstable modes, but it does not modify the main features of instability development.

Keywords: Liquid thin films ; Contact line ; Instability

---

1. Introduction

In this work we are concerned with the basic problem of the flow that develops during the covering of a solid surface by a thin liquid film. This flow con-

---

[*] Corresponding author.
E-mail address: jdiez@exa.unicen.edu.ar (J. Diez).
[1] Researcher of CONICET, Argentina.
[2] Fellow of CONICET, Argentina.

0167-2789/$ – see front matter © 2005 Elsevier B.V. All rights reserved.
doi:10.1016/j.physd.2005.06.026

figuration is present in a wide variety of technological problems, such as microchip production and microfluidic devices. This kind of flow develops as a balance between viscous and surface tension forces plus possibly a body force. The latter is often the main driving force and, depending on the application, it may be represented by gravity force [1–3], centrifugal force [4,5] or thermocapillary force [6–8].

We study here the spreading of a constant volume (CV) of fluid on a vertical plane. Initially, the fluid has the shape of a thin filament placed in horizontal position at the top of the substrate. Experiments with wetting fluids show that after some time the initially straight advancing frontline, where liquid, gas, and solid phase meet, becomes corrugated and then the flow evolves by forming well-defined rivulets (called fingers) separated by troughs. It is generally accepted that this instability is generated by perturbations along the strip and is related to the formation of a capillary ridge just behind the advancing the frontline. However, the analysis of the instability has only been done for the constant flux (CF) case, in which the fluid thickness far behind the frontline is kept constant (thus providing an unlimited supply of fluid).

In recent years many researchers have paid attention to this problem. On the experimental side, except by the work in [9,10], most of the authors have considered the CV case [1,11–14]. This is understandable considering that the CF case involves a more complex set-up. It must be noted that in the CV case, rather than the fluid volume, the cross sectional area of the initial condition is the characteristic parameter of the flow. The transversal extension is irrelevant since it is usually much larger than the flow extension in the streamwise direction. In contrast to above mentioned experiments for CV case, here we use much smaller areas, and thus the fluid spreads as a micrometric film. As a consequence, the flow studied here is more representative of the coating processes used in applications, and the corresponding experimental results are then also of particular interest to this field.

A detailed experimental study of the CV flow has been performed in [15]. Here, we extend that work by introducing numerical results for the description of the *complete* (linear and non-linear) evolution of the instability. For brevity, we consider a single experimental case, and compare it with the results of numerical simulations for both the stable and unstable stages of the spreading. The use of a linear model to predict the time evolution of the normal modes of the instability plays an important role in performing this comparison. This model (first developed in [15] and revisited here) is based on an adiabatic approximation of the thickness profile of the stable stage in the region around the capillary ridge. Since the model was previously validated by comparing its predictions to experiments, we use it now as a benchmark for our simulations.

A quantitative description of the experimental results is particularly difficult because the (observable) macroscopic flow is strongly affected by microscopic forces acting at the frontline. Thus, the flow description within the continuum hypothesis requires some assumptions in that region to avoid the inconsistency of the equations. One of these assumptions is the existence of an ultra thin precursor film at the moving contact line. This is the approach made in the simulations, and consequently it needs to be supported by the experimental observation.

The main purpose of this work is to show the capability of both linear models and numerical simulations to describe the frontline instability. To achieve this goal we use data from our own experiments [15] and a simulation code developed within the lubrication approximation. A description of the set-up and the basics of the optical diagnosis used in the experiments are briefly described in Section 2. The physical model and the numerical method employed to solve the flow within the lubrication approximation are presented in Section 3. Details of the numerical code as well as applications of this tool are reported in the literature [16–18]. Section 4 is devoted to the comparison of experiments and simulations in the stable stage. The nonlinear stage is discussed in Section 5, where we compare experiments and 2D simulations by post-processing the numerical results to mimic the experimental images. We also show that within the linear regime both the experimental and numerical results can be predicted by application of a linear growth model to the spectrum at a very early stage.

2. Problem description and experiment

The initial fluid configuration is a vertical filament flowing out from a small nozzle at the bottom of a

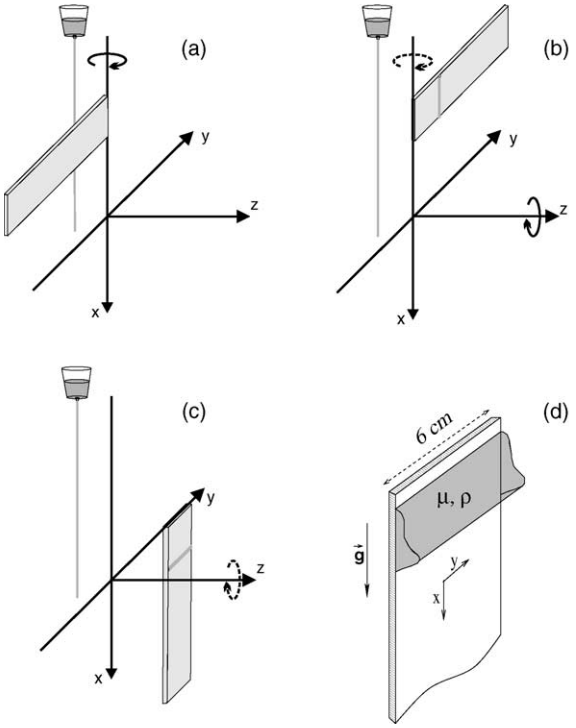

Fig. 1. Sketch of the mechanical system to place the fluid on the substrate. (a) Initial set-up and capture of the filament by the substrate. The circular arrows indicate the motions of the shaft (not drawn and coincident with *x*-axis) to which the frame with the glass is fixed. The shaft is hinged at the origin and the coordinate axes are fixed in space. (b) Filament on the substrate and intermediate position (dashed arrows indicate previous rotation). (c) Final position (the shaft coincides with *y*-axis). (d) Sketch of the constant volume spreading down the vertical substrate.

vessel filled with silicon oil (see Fig. 1a). Both the nozzle diameter and the fluid properties allow to control the value of the area A of the filament. We use polydymethilsiloxane (PDMS) with kinematic viscosity $\nu = 20\,St$, density $\rho = 0.96\,\mathrm{g\,cm^{-3}}$ and surface tension $\gamma = 19.8\,\mathrm{dyn/cm}$, so that the capillary length is $a = \sqrt{(\gamma/\rho g)} = 0.145\,\mathrm{cm}$.

The filament is captured on a glass (6 cm wide) by performing suitable rotations of its frame before reaching the final vertical position (see Fig. 1b and c). All these movements take about 1–2 s, i.e. a time interval which is very short compared to the time scale of the experiment (see below). The mechanism allows to obtain a fluid strip with contact lines which are both horizontal and straight, so that the initial configuration has a constant cross sectional area along the *y*-direction (see Fig. 1d).

The flow evolution is probed by two optical techniques: anamorphic lens and schlieren. The former is aimed to measure the thickness profile of the spreading, as well as the position of both contact lines. In this method the liquid film is impinged by a vertical light sheet and the optical system converts the in-plane deflections onto displacements on a perpendicular plane. This system consists of both a standard converging lens that forms a magnified image of the spreading region and an anamporhic lens [19]. The latter is equivalent to two crossed cylindrical lenses (one convergent and the other divergent) with focal lengths of equal magnitude, and with their axes at ±45° with respect to the *x*-axis (a cylindrical-spherical ophthalmic lens, conveniently chosen and oriented, does this job). The deflections produced with this system are related to the slope of the thickness profile of the probed fluid strip. During the early stage, the resulting data allow an accurate determination of the fluid volume after considering symmetry and integration of the profile. The constant value of the volume is checked by considering several profiles corresponding to different times. The other technique uses a schlieren method and is intended to describe the topography of the free surface and also the irregular shape of the frontline. Both techniques can be used simultaneously in our experimental set-up. Further details are presented in [15].

3. Lubrication equations and numerical code

Usually, thin film flow is studied within the lubrication approximation, i.e. small Reynolds number and small free surface slope. These hypotheses are satisfied in our experiments since PDMS oil is very viscous, and the strip is of small aspect ratio (typically, height/width <0.1). Thus, under the action of gravity and surface tension, the governing equation for the fluid thickness $h(x, y, t)$ is (see e.g. [20]):

$$3\mu\frac{\partial h}{\partial t} + \gamma\nabla\cdot(h^3\nabla(\nabla^2 h)) + \rho g\frac{\partial h^3}{\partial x} = 0, \qquad (1)$$

where $\mu = \nu\rho$ is viscosity, and g is gravity. The three terms in Eq. (1) stand for the viscous, capillary and gravitational forces, respectively. Here, x is the downhill coordinate.

Eq. (1) includes the non-slip boundary condition at the substrate surface. Due to the well known contact line paradox (macroscopic divergence of the viscous dissipation rate), all theoretical and computational methods require some regularizing mechanism: either assuming the existence of a thin precursor film of thickness h_f in front of the apparent contact line [21,2,22], or relaxing the no-slip boundary condition at fluid–solid interface by introducing a slipping length l_s [20,23,24]. An extensive comparison of these regularizing mechanisms applied to the spreading drop problem can be found in [25]. In that paper it is shown that the precursor film model leads to the results that are very similar to the ones obtained using slip model for $h_\mathrm{f} \approx l_\mathrm{s}$. Since the computational performance of the precursor model is much better, we use this model as a regularizing method in this work.

We have developed a numerical code to solve Eq. (1) both in its 1D version $h(x, t)$ as well as in its 2D version $h(x, y, t)$. The method uses centered finite difference for the spatial derivatives and the time discretization is performed by using implicit Crank-Nicholson scheme [18]. The solution is obtained in the domain $0 \le x \le L_x$ (and $0 \le y \le L_y$ in 2D case). The fluid volume under study is placed in the interval $x_{\mathrm{r}0} \le x \le x_{\mathrm{f}0}$, where $x_{\mathrm{f}0}$ and $x_{\mathrm{r}0}$ are the positions of the front and rear contact lines at $t = 0$, respectively, and the rest of the domain is filled with a thin (precursor) film of thickness h_f. Thus, the boundary condition at $x = 0, L_x$ are $h = h_\mathrm{f}$ and $\partial h/\partial x = \partial^3 h/\partial x^3 = 0$. These conditions are consistent with a continuous (and very small) inflow at $x = 0$ and the same outflow at $x = L_x$, and assure the mass conservation of the fluid bulk. In the 2D case, we impose mirror boundary conditions at the side walls, i.e. $\partial h/\partial y = \partial^3 h/\partial y^3 = 0$. Thus, the lines $y = 0, L_y$ represent symmetry planes.

Typically, the thickness of this film is one or two orders of magnitude smaller than the average bulk thickness. However, in order to produce results in *quantitative* agreement with the experiments we determine the appropriate value of h_f that reflects the actual physics of the contact line. This is done in the following Section by comparing numerical results for different values of h_f with the experimental thickness profiles. The comparison between 1D simulations and experiments shows that the resulting h_f is independent of A [15].

4. Stable stage: one dimensional flow

In the early stages of the spreading, the contact lines are straight and the flow is y-independent. Thus, the experimental profiles obtained in [15] can be compared with $h(x, t)$ from 1D simulations. A crucial element in reaching not only qualitative, but also quantitative agreement is to use an appropriate value of the precursor film thickness, h_f, in the simulations. These calculations require fine grids, because very thin precursor films demand very small step sizes, Δx, in order to achieve numerical convergence.

We obtain h_f by performing an iterative procedure. First, we choose two experimental thickness profiles, one close to the beginning of the spreading (t_a), and the other at a later time t_b (chosen small enough to ensure that the front is not yet corrugated). Then, we use the experimental profile at t_a as an initial condition in the numerical simulation, and we integrate it forward in time using appropriate initial guess for h_f. We then compare the computed and the experimental profile at t_b. Based on the difference between these two profiles, we choose the next iterate for h_f and repeat this procedure until convergence. The result of this iterative procedure is the value of h_f which produces very good *quantitative* agreement between computed and observed profiles: $h_\mathrm{f} = 43\,\mathrm{nm}$ (or $h_\mathrm{f} = 3 \times 10^{-5} a$). We have verified that this value of h_f is independent of the area A within the range $3 \times 10^{-4}\,\mathrm{cm}^2 < A < 15 \times 10^{-4}\,\mathrm{cm}^2$. Such a small value requires also very well resolved computations: We find that the results are fully converged for $\Delta x = 10^{-3} a$. We have also verified that this value of h_f remains unchanged if we choose a different t_b. We note that this h_f is in the range of the thicknesses measured and reported in the literature for precursor films (see [26,27]).

The experimental results for $A = 6.75 \times 10^{-4}\,\mathrm{cm}^2$ are shown in Fig. 2 (black dots). The evolution of the thickness profile starts with a shape resembling a cylindrical cap whose maximum is moving downwards (see Fig. 2a). During this stage, the frontline is practically straight. Later on, we observe the appearance of two regions (see Fig. 2b and c): the rear region, which acquires an almost parabolic shape, and the front region which evolves by developing a large bump. Fig. 2c shows a well developed profile when the frontline is about to start corrugating.

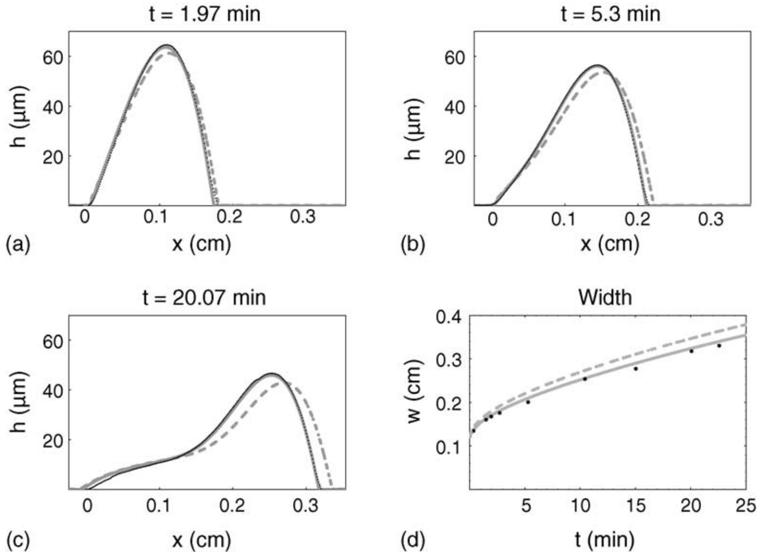

Fig. 2. (a)–(c) Thickness profiles at different times for $A = 6.75 \times 10^{-4}\,\mathrm{cm}^2$. Black dots correspond to experimental data. The solid and broken grey lines are numerical simulations for $h_\mathrm{f} = 3 \times 10^{-5}a$ and $h_\mathrm{f} = 10^{-4}a$, respectively. (d) Width of the film: experiments (black dots) and numerical simulations for $h_\mathrm{f} = 3 \times 10^{-5}a$ (grey solid line) and $h_\mathrm{f} = 10^{-4}a$ (grey broken line).

The grey lines in Fig. 2 correspond to the numerical simulations. We see that the results are in excellent agreement with the experimental data. The simulations are performed starting from the initial condition (cylindrical cap),

$$h(x, 0) = h_0(x) = h_\mathrm{max}\left[1 - \left(\frac{x - x_\mathrm{max}}{w_0/2}\right)^2\right], \qquad (2)$$

where $w_0 = x_\mathrm{f0} - x_\mathrm{r0}$ is the width of the strip in the streamwise direction at $t = 0$, $x_\mathrm{max} = (x_\mathrm{f0} + x_\mathrm{r0})/2$ is the central position of the maximum thickness h_max. Since both the values of w_0 and the area A are given by the anamorphic technique, we calculate $h_\mathrm{max} = 3A/2w_0$. We have verified that this initial shape leads to results that are in full agreement with those obtained by using an experimental profile for a given $t > 0$.

In Fig. 2d we compare the numerical (grey lines) and experimental (black dots) results for the width of the film, $w(t) = x_\mathrm{f}(t) - x_\mathrm{r}(t)$. We use the width, w, instead of x_f in order to consider a quantity independent of the reference frame (except for the very first stages, x_r does not vary appreciably during the spreading). In order to show the sensitivity of the simulations with respect to the precursor film thickness, we also present in this figure the numerical width obtained with $h_\mathrm{f} = 10^{-4}a = 125\,\mathrm{nm}$ (dashed grey line). Even though this value is still within the range expected for a precursor film, we see clearly that the predicted behavior of $w(t)$ significantly differs from experiments, while the results for $h_\mathrm{f} = 43\,\mathrm{nm}$ are in very good agreement.

5. Unstable stage: two dimensional flow

5.1. Experimental results

In addition to the previous technique we also use a schlieren method to probe the spreading. A sliding mirror allows to switch between one technique and the other. The schlieren technique is used with a diaphragm centered at the focus of lens which forms the image of the spreading, which is illuminated by an expanded probing laser beam [15]. The images thus obtained show a pattern of dark and bright zones, which correspond to regions where the modulus of the gradient of the thickness is greater or smaller than a cut-off value, respectively. The cut-off varies with the diameter d of the diaphragm (all photos presented here have $d \approx 1\,\mathrm{mm}$).

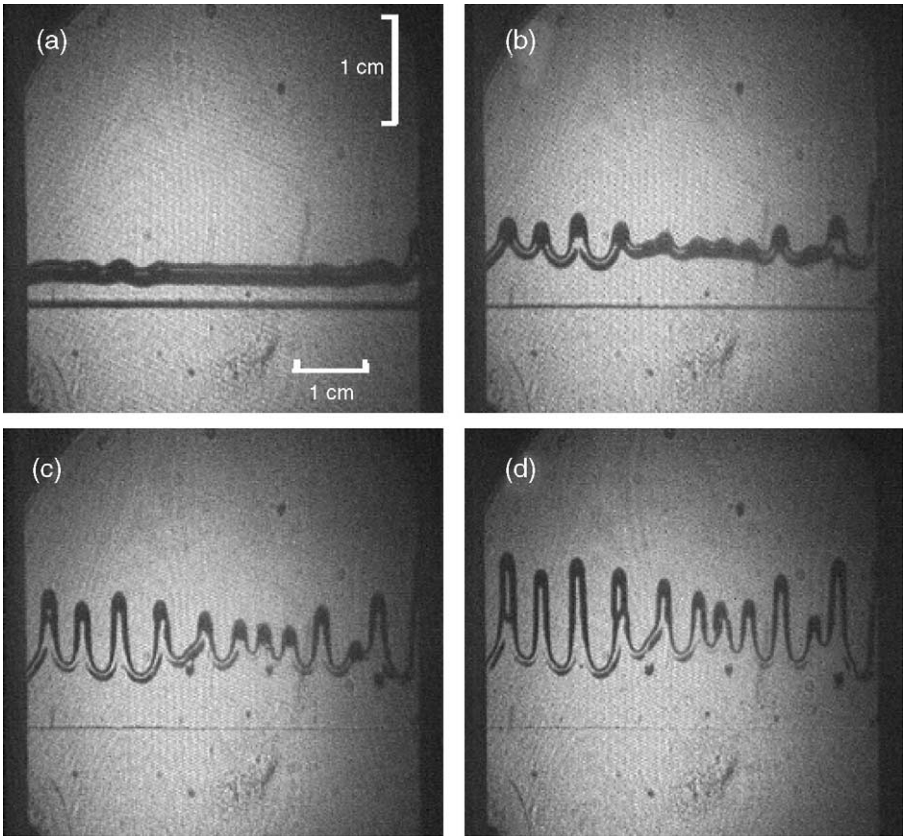

Fig. 3. Evolution of the film using the schlieren technique at: (a) $t = 38.2$, (b) 101.2, (c) 207.5 and (d) 343.7 min. The white segments show the length scale (1 cm) at the substrate.

Fig. 3 shows four typical images obtained by using this technique (the images are inverted by the optical system). We see clearly the formation of a pattern of fingers and troughs. The analysis of the instability pattern is performed by calculating the discrete Fourier transform (DFT) of the frontline for different times. In Section 5.2 we will compare the power spectra thus obtained with a linear model for the instability developed assuming a decomposition in normal modes.

In summary, the experimental results suggest the existence of stages in the development of the instability. These stages can be defined as follows:

- The first stage ($0 \leq t \leq t_0^*$) is characterized by a transient behavior in which the flow evolves from an initial condition (close to a cylindrical cap) to a structure with a parabolic shape in the rear region and a bump developed in the frontal region. Also, in this stage the frontline is still straight and does not show any appreciable corrugation. A more precise definition of t_0^* will be given below.
- Once the bump structure is clearly attained, the small perturbations tend to grow (unstable profile). In other words, the presence of the bump is a key feature for the development of the instability. For this stage, $t > t_0^*$, we develop in next Section a model for the growth of the amplitude of the perturbations within the linear approximation.
- When the amplitude of the perturbations exceeds a certain limit, the nonlinear effects become significant ($t > t_{\mathrm{NL}}$). However, in our experiments, these effects do not change the mean separation between fingers.

We emphasize that the instability develops *after* the formation of the bump (this was also verified for all cross-sectional areas explored in [15]). In particular, as A is increased, the instability develops faster, but the formation of the bump proceeds on a faster time scale as well. This observation constitutes an important difference with respect to other experiments performed with millimetric (or even thicker) films [1,14]. These films often include a rolling motion ('nose') at the advancing front, which stabilizes the flow and is responsible for the initial stable stage [28]. As the fluid thins surface tension effects become increasingly important, and the 'nose' changes its shape to a wedge-shape profile [29]. Later on, the front region grows a bump and the flow becomes unstable. Instead, in our experiments, there is no rolling stage, and the bump of the front region is present from the very early stages. However, the instability is not observed immediately, but it becomes apparent only after a certain time.

5.2. Linear model of the instability

In this Section we aim to develop a model for predicting the spatial spectrum of the instability, the growth rates of the perturbations and the value of the dominant wavelength λ_m. At present, there is no thorough analysis of the frontline instability for the constant volume problem. Instead, a fair amount of literature is devoted to the linear stability analysis of the constant flux problem. Here, we apply the results of the CF case to produce a predictive model for the CV configuration.

A major hindrance to performing the linear stability analysis of the unperturbed solution $h(x, t)$ for the CV case is the fact that the base solution is time dependent, as outlined above. We extend the linear stability analysis of the CF case by assuming that the base profile evolves sufficiently slowly relative to the growth rate of the perturbations (adiabatic approach).

Let us consider a profile $h(x, t_0)$ after the fluid starts spreading, with $t_0 \geq t_0^*$. Since at $t = t_0$ the flow has already developed a bump-plateau structure, we perform the analysis by perturbing the flow by a transverse corrugation characterized by a wavelength λ and an initial amplitude $I_0 = I(t_0)$. A key point in describing the linear evolution of the instability is to assume that the unperturbed state changes so slowly during this stage that the perturbation evolves on top of a quasi-steady base flow. Thus, the asymptotic growth rates of the CF case can be considered as the instantaneous growth rates of the CV case. This assumption requires that the amplitude of the perturbation be small enough, so not to modify significantly the base flow (linear regime). Therefore, every component of the spatial Fourier spectrum of the perturbation evolves independently from one another.

We attempt to approximate the bump region of the CV flow by the corresponding profile in the CF case with thickness h_p far from the front and the same h_f. The idea underlined in this approximation is that the instability basically depends on the thickness structure of this region, while the flow far behind does not affect the behavior of the front.

In the CF case, the translational invariance implies that the solution of the y-independent problem is of the traveling wave type. Thus, for a constant thickness, h_p, in the far region behind the front (plateau), we have a dimensionless solution of the form,

$$h = h_\mathrm{p} H(\xi), \qquad \xi = \frac{(x - ut)}{\ell}, \tag{3}$$

where

$$\ell = (a^2 h_\mathrm{p})^{1/3}, \qquad u = u_0(1 + b + b^2), \tag{4}$$

with $u_0 = \rho g h_\mathrm{p}^2 / 3\mu$ and $b = h_\mathrm{f}/h_\mathrm{p}$. In the linear stability analysis of this problem, it is assumed that there is a transverse perturbation of the base solution characterized by a wavelength λ. For a given b, there are two relevant wavenumbers: (a) k_max for which $\sigma(k_\mathrm{max})$ is the maximum, σ_max, and (b) $k^* = 2\pi/\lambda^*$, which yields $\sigma(k^*) = 0$ (marginal stability), such that the solution is unstable for $k < k^*$ ($\lambda > \lambda^*$), and stable otherwise. When the growth rates $\sigma(k)$ for several values b are plotted in the normalized form,

$$\frac{\sigma}{\sigma_\mathrm{max}} = F(q), \tag{5}$$

where $q = k/k^* = \lambda^*/\lambda$, they nearly collapse onto a single curve [15]. For the purpose of analyzing the CV case, we use a general functional form $q^2(1 - q^p)$ with p is a rational number. We find best agreement by using

$$F(q) = 95q^2(1 - q^{1/17}). \tag{6}$$

This fitting function is used here and it leads to $\lambda^* \approx 0.61\lambda_\mathrm{max}$. The departures from this function increases for $q > 1$, but the fitting in the unstable range is reasonably good, and it will be helpful in the model for CV case developed in the following Section.

As a consequence of the scaling given by Eq. (4), the characteristic time and length scale as $\ell/u_0 \approx h_\mathrm{p}^{-5/3}$ and $h_\mathrm{p}^{1/3}$, respectively (see e.g. [30]). Thus, the *instantaneous* growth rate in the CV case becomes [15]:

$$\sigma(q) = \sigma_\mathrm{max} h_\mathrm{p}^{5/3} F(q) \tag{7}$$

where $q = \lambda^* h_\mathrm{p}^{1/3}(t)/\lambda$, and $\lambda^* \approx 7.4$ is the critical wavelength for marginal stability of CF case. Here, $h_\mathrm{p}(t)$ and λ are expressed in units of the capillary length a, and t, σ are in units of $\tau = 3\mu a/\gamma$ and τ^{-1}, respectively. In order to avoid cumbersome notation, we use the symbols of the previous Section to denote the present dimensionless variables. The values of σ_max and λ^* expressed in these units are reported in [15].

The instantaneous growth rate satisfies $\sigma = I^{-1}\,\mathrm{d}I/\mathrm{d}t$, so we have:

$$I(\lambda, t) = I_0(\lambda) \exp\left(\int_{t_0}^{t} \sigma(q(t'))\,\mathrm{d}t'\right). \tag{8}$$

Thus, Eq. (7) allows us to calculate the instantaneous growth rate of the perturbation as a function of the dimensionless thickness $h_\mathrm{p}(t)$, and Eq. (8) predicts its amplitude.

To proceed we must define an appropriate way of determining the parameter $h_\mathrm{p}(t)$. For this purpose, let us consider a CF flow with a certain value h_p of the (asymptotic) flat region, such that it has a bump height h_b coincident with the one of the CV case with the same h_f. The idea is to approximate the CV flow by the solution of a CF case which fits the bump region the best. Note that this model is intended to describe only the instability of the frontline and not the complete flow in the CV problem. The underlined concept is that the instability basically depends on h_b and the slope at the frontline, and that other details of the flow are not so relevant.

5.3. Experiments versus linear model

The analysis of the instability pattern is performed by calculating the discrete Fourier transform of the images of the frontlines [15]. Fig. 4a–c shows both the experimental power spectra, $|v_\mathrm{s}(\lambda)|$, and the model

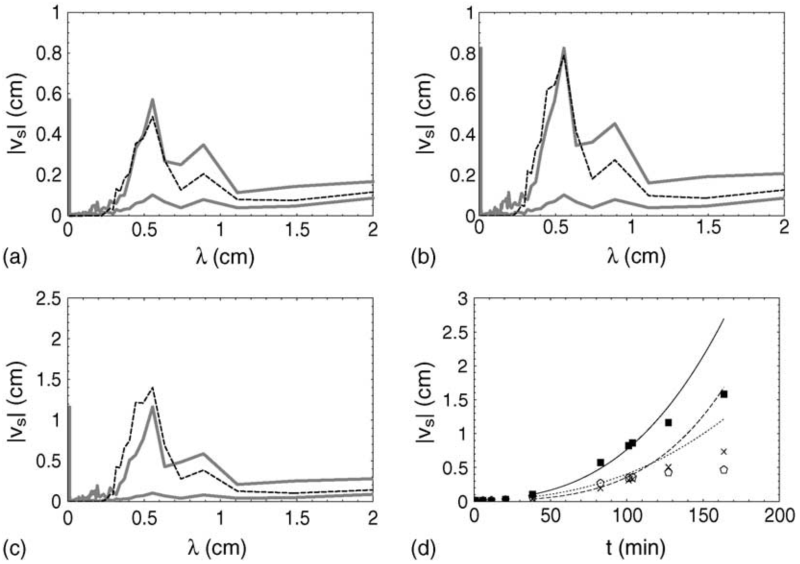

Fig. 4. Spectral evolution of the front line (see Fig. 3). (a) The lower and upper grey lines correspond to the experimental spectra at $t_0 = 38.2$ min and $t = 82.8$ min, respectively. The dashed line is the spectrum predicted by the model at t assuming a linear evolution from the spectrum at t_0. (b), (c) The same as (a) for final times $t = 101.2$ and 127.3, respectively. (d) Experimental (symbols) and model (lines) results for modal amplitudes versus time for $\lambda_\mathrm{max} = 0.55$cm (squares, solid line), $\lambda = 0.63$ cm (pentagons, dotted line) and $\lambda = 0.41$ cm (crosses, dashed line).

results at three times whose frontlines are presented in Fig. 3. The shape of the spectra is jagged due to the discrete character of the spectral analysis (DFT) in a finite spatial domain.

The model predictions are based on the linear evolution of the experimental spectrum $I_0(\lambda)$ from the earliest time $t_0 = 38.2$ min (lower grey line). These figures also present the spectra (dotted lines) obtained assuming constant initial amplitude, I_0. This constant is chosen as the experimental maximum at t_0, and therefore the dotted lines provide an envelope for the model results that use the details of experimental configuration at time t_0.

Fig. 4a and b, that concentrate on early times, show that close to the dominant wavelength $\lambda = \lambda_{\max} \approx 0.55$ cm, there is a very good agreement between the model and the experiment. Fig. 4c shows the results for later times. Since in DFT the difference between two consecutive wavenumbers is constant, the relative error of a given λ is inversely proportional to the corresponding wavenumber. For $\lambda_{\max}$ the error is approximately 12%. Although we observe an increasing departure of the growth rates from the linear model (dashed lines), the dominant wavelength given by the model is still close to the experimental one (solid line). One can expect that nonlinear effects account for this difference, since the shape of the frontline corresponding to these later times (see Fig. 3c and d) has the characteristic features of the nonlinear stage of the instability (e.g., the length of fingers is much larger than their separation). Another signature of nonlinear effects can be traced to the increased amplitudes of short wavelengths for late times. To see this, note that the experimental spectra show that the amplitudes for $\lambda < \lambda^*$ are not as small as one would expect based on the linear stability analysis. Our interpretation is that part of the energy of the linear modes is transferred by nonlinear processes to shorter wavelengths (energy cascade). Essentially, what occurs here is that the fingers' shape change for later times, becoming more pointing with parallel sides. Description of these features then requires shorter wavelengths. This mechanism subtracts energy from the dominant wavelengths and it may then be another source of the difference between the experimental results and the linear model for late times.

For very long wavelengths ($\lambda > 1.5$ cm), the experimental spectra have relatively high amplitudes. These wavelengths may be affected by the boundaries, due to the finite extension (in the y-direction) of the film. Nevertheless, these effects do not influence the behavior of the dominant wavelength, since $\lambda_{\max}$ is much smaller than the lateral width of the experimental domain.

Fig. 4d presents another test of the model. This figure compares the model predictions for the time evolution of modal amplitudes extracted from the experimental spectra shown in Fig. 3. We have chosen the amplitudes of the dominant wavelength, $\lambda_{\max}$, and of two other λ's (a shorter one and a longer one). For early times, the agreement between the model and the experiment is very good. For late times, which start close to $t = 120$ min, there is an increasing departure from the linear model predictions.

5.4. Numerical simulations versus linear model

In this section we present results of the numerical solution of the 2D version Eq. (1). In particular, we simulate the evolution of the instability of the experiment reported in Section 5.1. In order to mitigate effects due to the finite width of the domain, we set $L_y = 25a$, so that the mirror boundary conditions at $y = 0$ and L_y do not play an essential role in the flow evolution. For the maximum extension along x-direction we take $L_x = 8a$.

In order to choose the size of the grid steps, Δx and Δy, one must verify that the numerical calculation has converged for the given value of the precursor thickness, h_f. In Section 4 we find that $h_\mathrm{f} = 3 \times 10^{-5}a$ leads to a good agreement between experiments and simulations for the 1D stable stage. This value of h_f requires $\Delta x = 10^{-3}a$ to achieve convergence in the calculations. For the unstable stage, which requires the use of 2D simulations, this value of the grid step would give a mesh of 2×10^8 cells. Since this number exceeds our computational facilities, we must perform calculations with a coarser mesh, and consequently, we are forced to use a lager h_f. The results obtained with $\Delta x = 0.02a$ and $\Delta y = 0.05a$ are reasonably close to convergence for $h_\mathrm{f} = 10^{-4}a$, and thus we have a mesh with 2×10^4 cells (for a detailed study of the numerical method see [18]).

We perform calculations for the unstable stage of the reported experiment ($A = 6.75 \times 10^{-4}\,\mathrm{cm}^2$) by perturbing the flow in two different ways at $t = 0$:

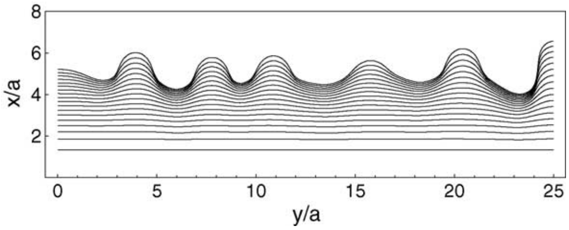

Fig. 5. Frontline evolution obtained numerically by *perturbing the vertex* of the initial cylindrical cap (see also Fig. 3). The lines correspond to times: $t/t_c = 0, 1, 2, \ldots, 17 \times 10^3$.

(1) The initial condition of the simulation is obtained by perturbing the thickness of the profile $h_0(x)$ given by Eq. (2). Along y-direction we use a collection of modes $\lambda_i = 2L_y/i$ $(i = 1, 2, \ldots, N)$ with random amplitudes A_i in the range $[-5, 5] \times 10^{-4}a$. The maximum of the perturbation is at the vertex of the parabola $h_0(x)$ and we set a Gaussian decay towards the front and rear contact lines. Thus, we write

$$h(x, 0) = h_0(x) - \delta(y) \exp\left[-\left(\frac{x - x_{\max}}{\sigma w_0}\right)^2\right], \qquad (9)$$

where

$$\delta(y) = \sum_{i=1}^{N} A_i \cos\left(\frac{2\pi y}{\lambda_i}\right), \qquad (10)$$

$x_{\max}$ is the position of the maximum of $h_0(x)$ (vertex) and σ controls the rate of spatial decay of the perturbation (here we use $\sigma = 0.1$ and $N = 50$).

Fig. 5 shows the time evolution of the frontline obtained from the simulations. Here, the space coordinates and time are in units of a and $t_c = 3\mu a/\gamma = 7.04 \times 10^{-3}$ min, respectively. We observe that, in agreement with experiments, the early (linear) evolution of the perturbation determines the position of fingers and troughs.

Since the model developed in Section 5.2 has proved successful to describe the linear instability of the experiments (see also [15]), we use it here as a benchmark for our numerical simulations. Note that we resort to this approach due to the above mentioned difficulties in performing calculations with the (small) value of the precursor film required for a quantitative description of the experimental results. In order to perform this check of consistency, we apply the model starting from an early numerical power spectrum and obtain the evolved spectrum at a later time. Then, we compare it with the corresponding numerical spectrum. This comparison is shown in Fig. 6 for $h_f = 10^{-4}a$ in both the model and the simulations. The solid lines are the results of the numerical code: the lower ones correspond to an early time ($t/t_c = 2000$) and the upper ones to a later time. The dashed lines are the predictions of the model. We see that even though there are two peaks for $t/t_c = 4000$ and 6000, the one with smaller wavelength ($\lambda_{\max} = 0.598$ cm) finally prevails (the relative error of $\lambda_{\max}$ is similar to the experimental one). There is a very good agreement between the simulations and the model not only in the value of $\lambda_{\max}$, but also in the growth rates of the dominant mode. The agreement is better for wavelengths close to $\lambda_{\max}$ than for longer ones [15].

(2) The second initial condition is also based on $h_0(x)$ but instead of perturbing the thickness of the

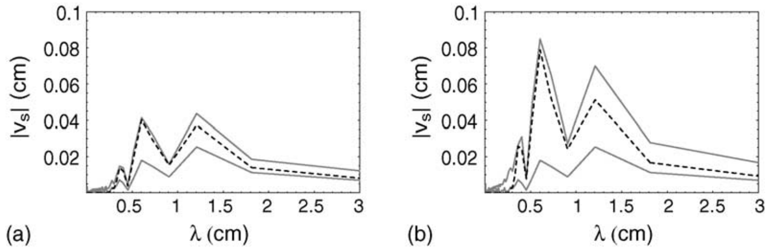

Fig. 6. Comparison between Fourier spectra of the frontlines obtained in numerical simulations performed by *perturbing the vertex* of the initial cylindrical cap (grey lines) and those predicted by the model (dashed lines). The lower grey line corresponds to $t = 2000\,t_c$. Both upper grey and dashed lines are at: (a) $t = 4000\,t_c$ and (b) $t = 6000\,t_c$.

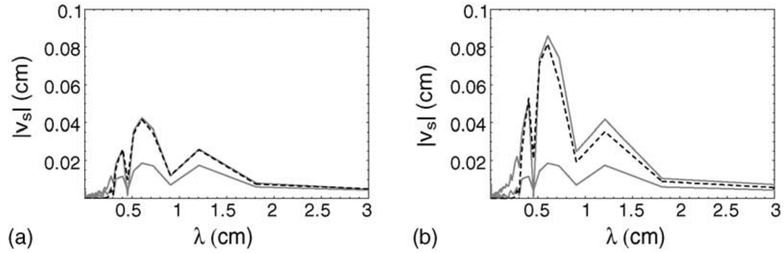

Fig. 7. Comparison between Fourier spectra of the frontlines obtained in numerical simulations performed by *perturbing the contact lines* of the initial cylindrical cap (grey lines) and those predicted by the model (dashed lines). The lower grey line corresponds to $t = 2000\,t_c$. Both upper grey and dashed lines are for: (a) $t = 4000\,t_c$ and (b) $t = 6000\,t_c$.

cylindrical cap, we perturb both contact lines along y-direction by small x-displacements $\delta(y)$ (see Eq. (10)). Thus, the initial position of the front is given by $x_f(y) = x_{f0} - \delta(y)$, where x_{f0} is the front position of $h_0(x)$.

The comparison between the power spectra given by the simulation and the model is shown in Fig. 7 at $t/t_c = 4000$ and 6000. In this case, the agreement is also satisfactory and the dominant wavelength is $\lambda_{\max} = 0.587$ cm. Note that in spite of using the same random amplitudes $\delta(y)$ in both numerical cases, the resulting spectra, Figs. 6 and 7, differ in detail, but they share the same dominant wavelength.

In summary, for two different ways of triggering the instability we observe the same basic features in the power spectra: the initial development of two peaks and the final predominance of the one with the shorter wavelength, $\lambda_{\max} \approx 0.59$ cm. Independently of how the instability is triggered, the evolution of the modal amplitudes are very well described by the model during the linear stage.

5.5. *Experiments versus 2D numerical simulations*

In spite of the impossibility of performing 2D numerical simulations for the value of h_f estimated in the 1D stable stage ($h_f = 3 \times 10^{-5}a$), we compare here the experimental results with those of the 2D simulations with $h_f = 10^{-4}a$. We explore which features of the experiment can still be reproduced by the simulations, despite different h_f.

Fig. 8a shows a region of the schlieren picture at $t = 101.2$ min (see also Fig. 3b). The size of this region coincides with that of the domain in the 2D simulations. In order to make a comparison with the experiment, we perform on $h(x, y, t)$ the same procedure that the schlieren technique produces on the light rays deviated by the liquid free surface (the slopes $\partial h/\partial x$ and $\partial h/\partial y$ are related to the deviation angle by Snell's law). Fig. 8b and c show the computational results for the contour plots of $|\nabla h|$ at the same time as the experiment, where the zones with $|\nabla h|$ less than a certain cut-off are shown in black. The cut-off value is obtained by using the values of the focal lenses and the diameter of the pinhole used in the experiment. Fig. 8b corresponds to the simulation obtained by perturbing the vertex of the cylindrical cap at $t = 0$, while Fig. 8c is for the perturbation at the frontline. Clearly, the zones of large $|\nabla h|$ (near the tips and at the rims of the troughs) are in agreement with the experiment. Due to the larger value of h_f used in the simulations, the development of the instability is slowed down with respect to the experiment, and consequently, the ondulated frontlines shown in Fig. 8b and c have not yet developed longer fingers. However, both figures show the same features as the experiment, such as the position of main fingers and the average distance between them. Note also that the perturbations used in the simulations are arbitrary and are not related to the unknown (uncontrollable) perturbations that trigger the instability in the experiment.

In Fig. 9 we compare the numerical and experimental Fourier spectra at $t = 83$ min. As expected, due to the thicker precursor used in the calculations, the numerical modal amplitudes are smaller than the experimental ones. However, the dominant wavelength given by the simulations, $\lambda_{\max} = 0.59$ cm, is very close to the experimental value, $\lambda_{\max} = 0.55$ cm. Therefore, we

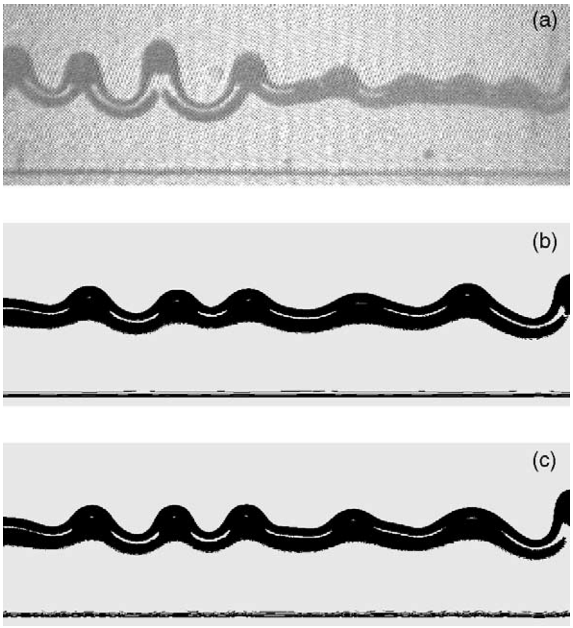

Fig. 8. (a) Experimental schlieren picture for $t = 101.2$ min. (b)–(c) Computational results where an analogous procedure (i.e., zones of $|\nabla h|$ less than a cut-off are shown in black) at the same time as in experiment, obtained by perturbing the vertex (b), and the contact lines (c) of the cylindrical cap at $t = 0$.

conclude that the simulations reproduce very well the average distance between the patterns, which is one of the main characteristics of instability development. It should be noted that the amplitude of the perturbations imposed at the vertex (case (a)) are much smaller than those imposed at the contact lines (case (b)). Since both cases lead to very similar amplitudes at a given time, this suggests that the vertex of the initial condition is more sensitive to perturbations than the contact lines.

6. Summary and conclusions

In this work we present a detailed comparison of experimental results and simulations of the spreading of a constant volume of fluid down a vertical glass substrate. For the sake of brevity, we restrict the discussion to a single experimental case and compare the experimental data with both the results of 2D simulations and the predictions of a linear model of the instability development.

We show results of an experimental spreading of a constant volume of PDMS oil down a vertical glass substrate. An anamorphic lens technique yields the thickness profile and the width of the film in the stable stage of the experiment. We use the results to precisely determine the thickness of the precursor film by comparing the evolution of the experimental profiles with 1D numerical simulations. The obtained thickness is 43 nm, consistent with the results reported in the literature. The schlieren technique is used to study the shape of the frontline after the onset of the instability by performing a discrete Fourier transform of the fluid frontlines. The resulting spatial spectra show a dominant wavelength which is determined in the linear stage of the instability development, and is maintained during the non-linear stage.

A semi-analytical model, previously developed in [15], is revisited for completeness. It successfully gives the amplitude evolution of the normal modes of the instability. Although its validity is restricted to the linear stage, its predictions are relevant since at this stage the fate of each mode is determined. In addition, this model is very useful to bridge experiments and simulations. An issue is that a direct comparison between experiments and simulations is difficult, since this would require very demanding computations. In fact, the use

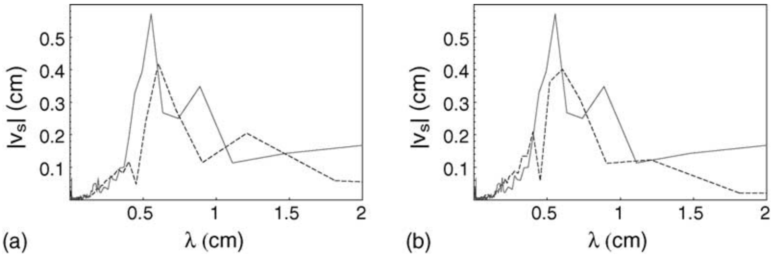

Fig. 9. Comparison between Fourier spectra of the frontlines obtained in numerical simulations (dashed lines) and the experimental one (solid lines) at $t = 83$ min. We perturb (a) the *vertex* of the initial cylindrical cap, and; (b) the *contact lines* of the initial cylindrical cap.

of the value of h_f that was found to precisely model the experiment in the stable stage, would demand a very fine grid (of the order of 2×10^8 cells). Thus, instead of trying to relate directly experiments and simulations, we verify the consistency of the numerical results by comparing with the model that uses a thicker precursor. These simulations also show that the main features of the emerging spectrum are independent of the details of the imposed perturbations. The results confirm that, except for some decrease of the growth rates, the numerical approach that uses a thicker precursor accurately describes the frontline instability.

Acknowledgments

A.G.G., J.D., J.G. and R.G. acknowledge support from Consejo Nacional de Investigaciones Científicas y Técnicas (CONICET-Argentina) and Agencia Nacional de Promoción Científica y Tecnológica (Argentina, grant PICTR 2002-0094). L.K. acknowledges support from NSF grant no. INT-0122911. J.D. acknowledges support from CONICET grant PEI 6304.

References

[1] H. Huppert, Flow and instability of a viscous current down a slope, Nature 300 (1982) 427.

[2] A.L. Bertozzi, M.P. Brenner, Linear stability and transient growth in driven contact lines, Phys. Fluids 9 (1997) 530.

[3] L.W. Schwartz, Viscous flows down an inclined plane: Instability and finger formation, Phys. Fluids A 1 (1989) 443.

[4] N. Fraysse, G.M. Homsy, An experimental study of rivulet instabilities in centrifugal spin coating of viscous Newtonian and non-Newtonian fluids, Phys. Fluids 6 (1994) 1491.

[5] F. Melo, J.F. Joanny, S. Fauve, Fingering intability of spinning drops, Phys. Rev. Lett. 63 (1989) 1958.

[6] A.M. Cazabat, F. Heslot, S.M. Troian, P. Carles, Finger instability of this spreading films driven by temperature gradients, Nature 346 (1990) 824.

[7] M.J. Tan, S.G. Bankoff, S.H. Davis, Steady thermocapillary flows of thin liquid layers. I. Theory, Phys. Fluids A 2 (1990) 313.

[8] X. Fanton, A.M. Cazabat, D. Quéré, Thickness and shape of films driven by a Marangoni flow, Langmuir 12 (1996) 5875.

[9] M. F. G. Johnson. Experimental study of rivulet formation on an inclined plate by fluorescent imaging, Ph.D. thesis, Northwestern University, 1997.

[10] M.F.G. Johnson, R.A. Schluter, S.G. Bankoff, Fluorescent imaging system for global measurement of liquid film thickness and dynamic contact angle in free surface flows, Rev. Sci. Instrum. 68 (1997) 4097.

[11] N. Silvi, E.B. Dussan V, On the rewetting of an inclined solid surface by a liquid, Phys. Fluids 28 (1985) 5.

[12] J.R. de Bruyn, Growth of fingers at a driven three–phase contact line, Phys. Rev. A 46 (1990) 4500.

[13] J.M. Jerrett, J.R. de Bruyn, Finger instability of a gravitationally driven contact line, Phys. Fluids A 4 (1992) 234.

[14] H.-C. Chang, I. Veretennikov, A. Indeikina, Front dynamics and fingering of a driven contact line, J. Fluid. Mech. 373 (1998) 81–110.

[15] A.G. González, J. Diez, J. Gomba, R. Gratton, L. Kondic, Spreading of a thin two-dimensional strip of fluid on a vertical plane: Experiments and modeling, Phys. Rev. E 70 (2004) 026309.

[16] J. Diez, L. Kondic, Contact line instabilites of thin liquid films, Phys. Rev. Lett. 86 (2001) 632.

[17] L. Kondic, J. Diez, Contact line instabilities of thin film flows: Constant flux configuration, Phys. Fluids 13 (2001) 3168.

[18] J. Diez, L. Kondic, Computing three-dimensinal thin film flows including contact lines, J. Comp. Phys. 183 (2002) 274.

[19] L. Thomas, R. Gratton, B. Marino, S. Betelu, J. Diez, J. Simon, Measurement of the slope of an unsteady liuid surface along a line by an anamorphic schlieren system, Measure. Sci. Technol. 7 (1996) 1134.

[20] H.P. Greenspan, On the motion of a small viscous droplet that wets a surface, J. Fluid Mech. 84 (1978) 125.

[21] S.M. Troian, E. Herbolzheimer, S.A. Safran, J.F. Joanny, Fingering instabilities of driven spreading films, Europhys. Lett. 10 (1989) 25.

[22] M.A. Spaid, G.M. Homsy, Viscoelastic free surface flows: spin coating and dynamic contact lines, J. Non-Newtonian Fluid. Mech. 55 (1994) 249.

[23] E.B. Dussan V, The moving contact line: the slip boundary condition, J. Fluid Mech. 77 (1976) 665.

[24] L.M. Hocking, A.D. Rivers, The spreading of a drop by capillary action, J. Fluid. Mech. 121 (1982) 425.

[25] J. Diez, L. Kondic, A.L. Bertozzi, Global models for moving contact lines, Phys. Rev. E 63 (2001) 011208.

[26] P.G. de Gennes, Wetting: Statics and dynamics, Rev. Mod. Phys. 57 (1985) 827.

[27] R. Gratton, J.A. Diez, L.P. Thomas, B. Marino, S. Betelú, Quasi-self-similarity for wetting drops, Phys. Rev. E 53 (1996) 3563.

[28] R. Goodwin, G.M. Homsy, Viscous flow down a slope in the vicinity of a contact line, Phys. Fluids A 3 (1991) 515.

[29] B.M. Marino, L.P. Thomas, J.A. Diez, R. Gratton, Capillarity effects on viscous gravity spreading of wetting fluids, J. Colloid Interface Sci. 177 (1996) 14.

[30] Y. Ye, H. Chang, A spectral theory for fingering on a prewetted plane, Phys. Fluids 11 (1999) 2494.